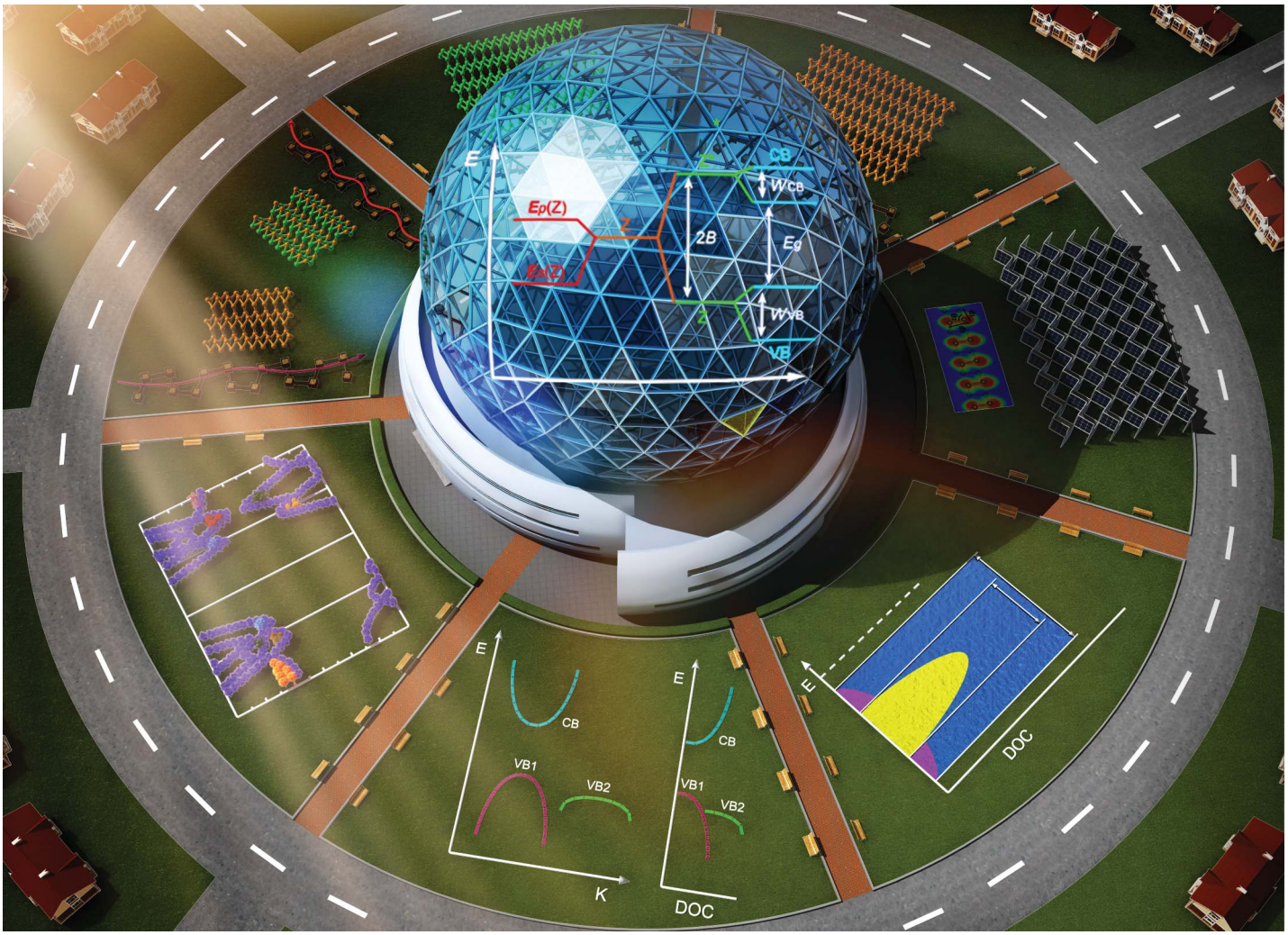

Showcasing a study on approaching two-dimensional thermoelectric material design by using a chemical intuition by Mr Bo Peng and Prof. Hao Zhang at Fudan University.

Chemical intuition for high thermoelectric performance in monolayer black phosphorus, α-arsenene and aW-antimonene

Identifying materials with high thermoelectric performance remains a challenge. Using a chemically intuitive approach based on the bond-orbital theory, three anisotropic 2D group-V materials (black phosphorene, α-arsenene, and aW-antimonene) are identified as candidates for high thermoelectric energy conversion efficiency.

As featured in:

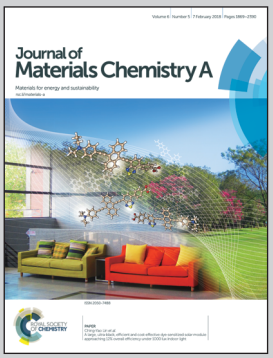

See Hao Zhang *et al.*, *J. Mater. Chem. A*, 2018, **6**, 2018.

ROYAL SOCIETY OF CHEMISTRY

rsc.li/materials-a

Registered charity number: 207890

Journal of Materials Chemistry A

PAPER

View Article Online
View Journal | View Issue

Cite this: J. Mater. Chem. A, 2018, 6, 2018

Chemical intuition for high thermoelectric performance in monolayer black phosphorus, α-arsenene and aW-antimonene

Bo Peng,[a] Hao Zhang,*[ac] Hezhu Shao,[b] Ke Xu,[a] Gang Ni,[a] Jing Li,[a] Heyuan Zhu[a] and Costas M. Soukoulis[cd]

Received 27th October 2017
Accepted 19th November 2017

DOI: 10.1039/c7ta09480a

rsc.li/materials-a

Identifying materials with intrinsically high thermoelectric performance remains a challenge even with the aid of a high-throughput search. Here, using a chemically intuitive approach based on the bond-orbital theory, three anisotropic 2D group-V materials (monolayer black phosphorus, α-arsenene, and aW-antimonene) are identified as candidates for high thermoelectric energy conversion efficiency. Concepts, such as bond length, bond angle, and bond strength, are used to explain the trends in their electronic properties, such as the band gap and the effective mass. Our first principles calculations confirm that high carrier mobilities and large Seebeck coefficients can be obtained at the same time in these materials, due to complex Fermi surfaces originating from the anisotropic structures. An intuitive understanding of how the bonding character affects phonon transport is also provided with emphasis on the importance of bonding strength and bond anharmonicity. High thermoelectric performance is observed in these materials. Our approach provides a powerful tool to identify new thermoelectric materials and evaluate their transport properties.

1 Introduction

In any energy conversion process, there is always some energy wasted as heat. At present, about two-thirds of the utilized energy worldwide is wasted in the form of heat, stimulating efforts to capture this wasted heat to generate emission-free electricity for both environmental and economic reasons. Thermoelectric materials convert heat directly into electricity. However, one main challenge of implementing thermoelectric energy conversion in commercial applications is the low efficiency of thermoelectric materials. The performance of thermoelectric materials is quantified by the thermoelectric figure of merit[1–3]

$$zT = \frac{\sigma S^2 T}{\kappa}, \quad (1)$$

where σ is the electrical conductivity, S is the Seebeck coefficient measuring the electrical potential difference created from a temperature gradient, and κ is the thermal conductivity approximated by the combination of the electronic and lattice thermal conductivity, $\kappa = \kappa_{el} + \kappa_L$. The optimization of zT is difficult because of the conflicting trends in σ, S, and κ. For instance, increasing σ usually indicates lowering S, while κ_{el} is proportional to σ according to the Wiedemann–Franz relation.[4] Moreover, reducing κ_L without sacrificing electrical transport properties remains a problem, due to the strong interdependence between electrical and thermal transport.

Approaches for achieving high thermoelectric performance include improving carrier mobility by modulation doping,[5] enhancing the Seebeck coefficient by band convergence and the introduction of resonance states,[6] reducing thermal conductivity with nanostructures,[7] adding a new degree of freedom by defect engineering,[8] and creating electron-crystal phonon-glass structures.[9] Another strategy is to identify materials with intrinsically high thermoelectric performance.[10,11] Recently, computational material techniques have been developed to perform a high-throughput *ab initio* search for materials with intrinsically high thermoelectric performance.[12–14] In addition, techniques in the field of information science, such as compressive sensing, can be used to generate *ab initio* training data and select physically important terms in thermoelectric performance.[15] However, the main disadvantage of these approaches is being non-intuitive. A comprehensive understanding of intrinsic properties, such as effective mass, band gap, electron scattering, and phonon scattering, can be exploited to accelerate the optimization of thermoelectric transport properties. Considering a chemical point of view, these properties rely on the structural chemistry of a material. The key issue is an intuitive understanding of how the

[a]Department of Optical Science and Engineering, Key Laboratory of Micro and Nano Photonic Structures, Ministry of Education, Fudan University, Shanghai 200433, China. E-mail: zhangh@fudan.edu.cn

[b]Ningbo Institute of Materials Technology and Engineering, Chinese Academy of Sciences, Ningbo 315201, China

[c]Department of Physics and Astronomy and Ames Laboratory, Iowa State University, Ames, Iowa 50011, USA

[d]Institute of Electronic Structure and Laser (IESL), FORTH, 71110 Heraklion, Crete, Greece

bonding character affects electrical and phonon transport, which provides a simple, but quanlitative, perspective on thermoelectric performance.[1]

Other than the non-intuitive methods, this understanding approaches thermoelectric material design using the chemical intuition provided by bond-orbital theory and a classic understanding of bond length, structure, strength and anharmonicity.[1] Here we extend this intuitive idea to the family of 2D materials. Three materials, monolayer black phosphorus, α-arsenene, and aW-antimonene, are identified to have potentially high thermoelectric performance using chemical intuition. Both their electrical and phonon transport properties are explored by first-principles calculations and the Boltzmann transport equation for electrons and phonons.[16,17] These can be understood by structural chemistry, especially chemical bonding. This chemical approach by thinking about bonding interactions provides a new strategy to find new thermoelectric materials and can be integrated into a high-throughput search, as we will develop in the future.

2 Chemical intuition

We address challenges such as how to evaluate the band gap and engineer the effective mass by employing a simplified bonding model. Materials with suitable electronic structures for thermoelectric applications must be non-polar, with large bond length and anisotropic structure. After setting the benchmark for thermoelectric materials, we take the family of 2D materials as an example to examine this chemically intuitive approach. Then we search among 2D materials to choose a system for exploration.

2.1 Simplified bonding model

Bond-orbital theory provides a simplified model of band structure evolution by the interactions of atomic orbitals using a chemical picture.[18] As shown in Fig. 1(a), in a polar solid with composition XY, atomic orbitals of element X and element Y hybridize with each other, leading to a bonding state XY and an antibonding state XY*. These bonding orbitals finally form bands. The linear combination of atomic orbitals (LCAO) provides a description of the electronic structure in an intuitive bonding picture. The band gap, E_g, is related to these bonding parameters:

(1) $2A$ is the energy difference between the atomic orbitals of X and Y. A represents the hybrid polar energy in the tight-binding approach.[18] The higher the electronegativity of an element, *i.e.*, larger ionization energy, the lower the energy of the atomic orbitals.[19] A larger difference in electronegativity between X and Y usually leads to a larger E_g.

(2) $2B$ corresponds to the bonding–antibonding splitting. $(B–A)$ is the bonding energy from the stabilization of the bonding orbital XY compared to the atomic orbital Y, and the destabilization of the antibonding orbital XY* compared to the atomic orbital X, respectively. B can be expressed as[18,20]

$$B = \sqrt{V^2 + A^2}, \quad (2)$$

where V is the hybrid covalent energy that reveals the strength of orbital overlap interactions.

(3) W_{VB} and W_{CB} are the width of the valence and conduction band, respectively. The band width increases with larger overlap of neighboring orbitals. This can be understood where the individual states are broadened into a band due to orbital overlap interactions.

The tight-binding approach offers a chemically intuitive description of the electronic structure, and is a useful tool to predict E_g without high-level calculations. Within the framework of the linear combination of atomic orbitals (LCAO) theory, the challenge of "What is the best electronic structure for thermoelectric materials?" can be addressed using the chemical understanding of bonding.

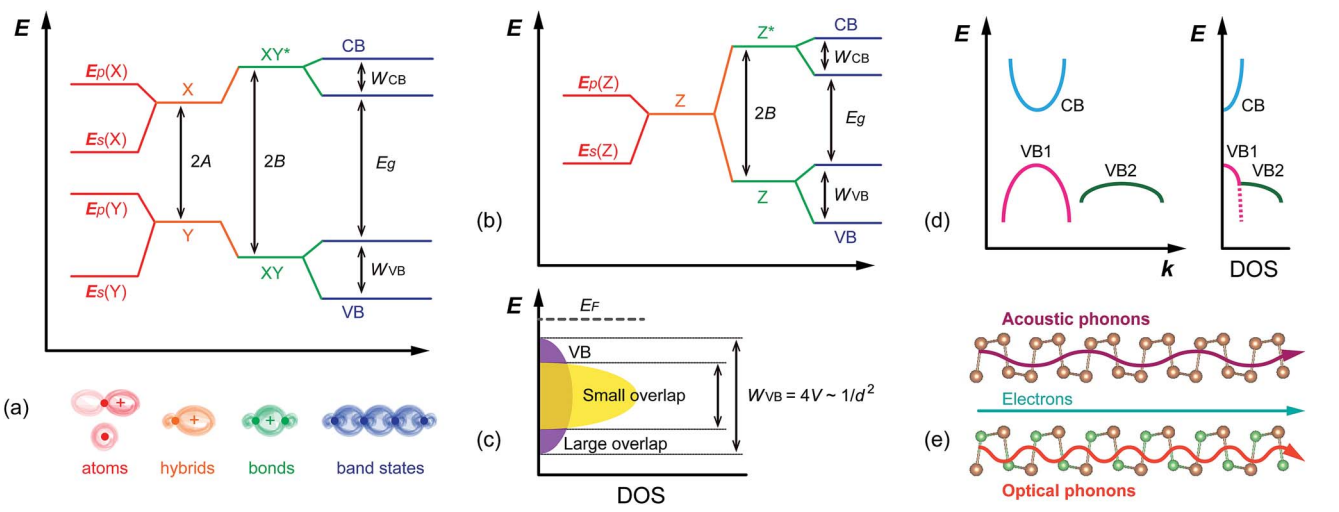

Fig. 1 Transformation of the LCAO, from atomic s and p orbitals to hybrids, to bond orbitals, and eventually to band states in (a) polar crystal XY and (b) non-polar crystal Z. (c) The broadening of the valence band increases with increasing orbital overlap, leading to a small DOS and a low m^*. (d) Configuration of the energy band and DOS of a multivalley semiconductor. (e) Scattering of carriers by acoustic phonons and polar optical phonons.

2.2 Best electronic structure for thermoelectric materials

Considering the optimum band gap for thermoelectric applications, it has been argued that the best materials should have a narrow band gap with high carrier concentration.[4] To suppress the contribution from minority carriers, an optimum band gap of 0.15–0.26 eV is required.[21,22] For polar compounds ($A \neq 0$), the bonding–antibonding splitting $2B = 2\sqrt{V^2 + A^2}$ is larger than that of non-polar materials ($A = 0$), leading to a larger E_g. Monolayer graphene and BN are typical examples of how the electronegativity difference influences E_g. Graphene and BN have the same planar structures and similar lattice constants, each with eight valence electrons in the unit cell. In addition to the covalent character, monolayer BN also has a polar character in the bonds, *i.e.* $A \neq 0$, which results in a much larger E_g than graphene.[23] Fig. 1(b) shows the narrow E_g in non-polar crystals – preferred in thermoelectric materials.

In non-polar materials, eqn (2) becomes $B = V$. The strength of orbital coupling, V, decreases with increasing bond length, d,[24]

$$V \sim \frac{1}{d^2}. \quad (3)$$

Increasing d lowers the bonding strength by decreasing orbital overlap, which decreases the separation between the bonding and antibonding bands.[1] In 2D group-V materials with increasing bond length, the trend of E_g (P) > E_g (As) > E_g (Sb) > E_g (Bi) indicates how d influences the electronic structure.[25]

Besides A and V, the dispersion of the valence and conduction band, W_{VB} and W_{CB}, is critical to determine the electronic structure as well. Similar to V, the broadening of the band width, W, increases with increasing orbital overlap. The band width in 1D non-polar semiconductors is determined by V,[1]

$$W = 4V. \quad (4)$$

A strong overlap (small d) usually leads to a broad band, which results in a low effective mass, m^*, and a low density-of-states (DOS), as shown in Fig. 1(c). In contrast, a narrow band, due to long bonds, corresponds to a high m^* and a large DOS. Heavy carriers are easily localized and less mobile ($\mu = e\tau/m^*$). However, the Seebeck coefficient, S, is large at the edge of a heavy band.[3] Materials with high m^* possess large S, but low μ. This inherent trade-off is one of the main challenges in designing thermoelectric materials.

To overcome the trade-off, one approach is to take advantage of complex Fermi surfaces, such as high band degeneracy.[26] As shown in Fig. 1(d), the band shape of each Fermi surface pocket is unchanged, but a strong enhancement of the DOS can be induced. Thus, a large S can be achieved without sacrificing μ when intervalley scattering is neglected. The complex band structure is often exploited in anisotropic materials, such as SnSe.[11,27] In fact, anisotropic materials with anisotropic band masses can have the same effect and offer great opportunities to optimize the carrier mobility along the direction of low effective mass, while many states are available in the transverse direction.

Now, we look at the role of electronegativity. For polar compounds, E_g is determined by the hybrid polar energy A and the hybrid covalent energy V. Actually, V becomes less important as A increases.[1] This explains why monolayer BN has a similar d (1.45 Å) to graphene (1.42 Å), but much larger E_g (4.61 eV).[23] Similar to E_g, the dispersion, W, is determined by the electronegativity difference, A, rather than the overlap, V.[1] For the isoelectronic series Ge, GaAs, ZnSe, and CuBr, with increasing polarity, *i.e.* increasing electronegativity difference, the width of the valence band becomes progressively smaller.[28] Therefore, ionic materials usually possess large E_g and small W, leading to low mobility. In addition, a large electronegativity difference reduces the carrier mobility significantly by increasing the scattering from the polar optical phonons, as shown in Fig. 1(e). Therefore, we only consider non-polar crystals for thermoelectric candidates, hereafter.

2.3 Choosing a system for exploration

We search among 2D materials to find a suitable system for exploration after setting the benchmark for thermoelectric materials as follows: (1) non-polar, (2) large bond length, and (3) anisotropic structure. Considering electrical transport, the first rules out a large E_g and strong electron–optical phonon interaction, while the latter two can optimize σ and S. Considering phonon transport, large bond length leads to weak bonding strength and suppresses phonon transport, while the anisotropic structure creates tortuous phonon transport paths; hence, reduces κ.

We first eliminate the only synthesized group-III material borophene due to small d.[29,30] For 2D group-IV materials, graphene can be ruled out, due to small d as well, which results in ultrahigh thermal conductivity.[31,32] We also rule out other group-IV materials with both low-buckled and dumbbell structures because of their isotropic transport properties.[33–36] For the same reason, buckled group-V materials, such as nitrogene,[37] blue phosphorene,[38–40] β-arsenene,[25,41,42] and β-antimonene,[25,41–46] are not taken into consideration. Thus, anisotropic 2D group-V materials, such as monolayer black phosphorus,[47–51] α-arsenene,[25,41,42,52] and asymmetric washboard antimonene (aW-antimonene)[25,41–43] become the only remaining options.

In fact, monolayer black phosphorus has been shown to be a promising thermoelectric material recently[53–62] because of its extremely high hole mobility[51] and large Seebeck coefficient,[53] but the main challenge comes from its high lattice thermal conductivity.[63–71] *Via* chemical intuition, higher thermoelectric performance might be expected in α-arsenene and aW-antimonene. From P to As and to Sb, the bond length, d, increases, leading to a narrower V, hence, larger S. With similar puckered structures, anisotropic transport properties enable optimized S and σ. Furthermore, large d implies a weak bonding strength and, therefore, suppresses phonon transport. Therefore, a comprehensive study of the thermoelectric properties of monolayer black phosphorus, α-arsenene and aW-antimonene can provide a deep insight into the chemistry underlying thermoelectric performance.

3 Chemical bonding and electrical transport

Materials with large effective masses often possess large Seebeck coefficients, but low carrier mobilities. To optimize these

coupled electrical transport properties, a thorough understanding of the relationship between the chemical bonding and electronic properties is required. Using the chemical intuition provided by bond-orbital theory, our understanding of the electronic structures in monolayer black phosphorus, α-arsenene, and aW-antimonene is enhanced. Concepts, such as bond length, bond angle, and bond strength, are utilized to explain trends in electronic properties, such as the band gap, carrier effective mass, band degeneracy, and deformation potential. An intuitive understanding of how the bonding structure affects carrier mobility is provided. Benefiting from the anisotropic structure, the complex Fermi surfaces in these materials result in a large Seebeck coefficient, while maintaining a high carrier mobility.

3.1 Bond length and electronic structure

In non-polar materials, both the band gap and band width are determined by the bond length, d, because it reflects the strength of orbital coupling. In anisotropic 2D group-V materials, there are two types of bonds within and between the sublayer or sublayers. The d of these two types of bonds implies the strength of the σ and π orbitals, which further influence the magnitude and position of the band gap.

As shown in Fig. 2(a) and (b), monolayer black phosphorus has a puckered orthorhombic structure.[74] The optimized geometries of monolayer black phosphorus, α-arsenene, and aW-antimonene are listed in Table 1 – consistent with other theoretical studies.[42,43,51,52,72,73,75,76] Monolayer black phosphorus has two sublayers including two types of bonds. The shorter d_1

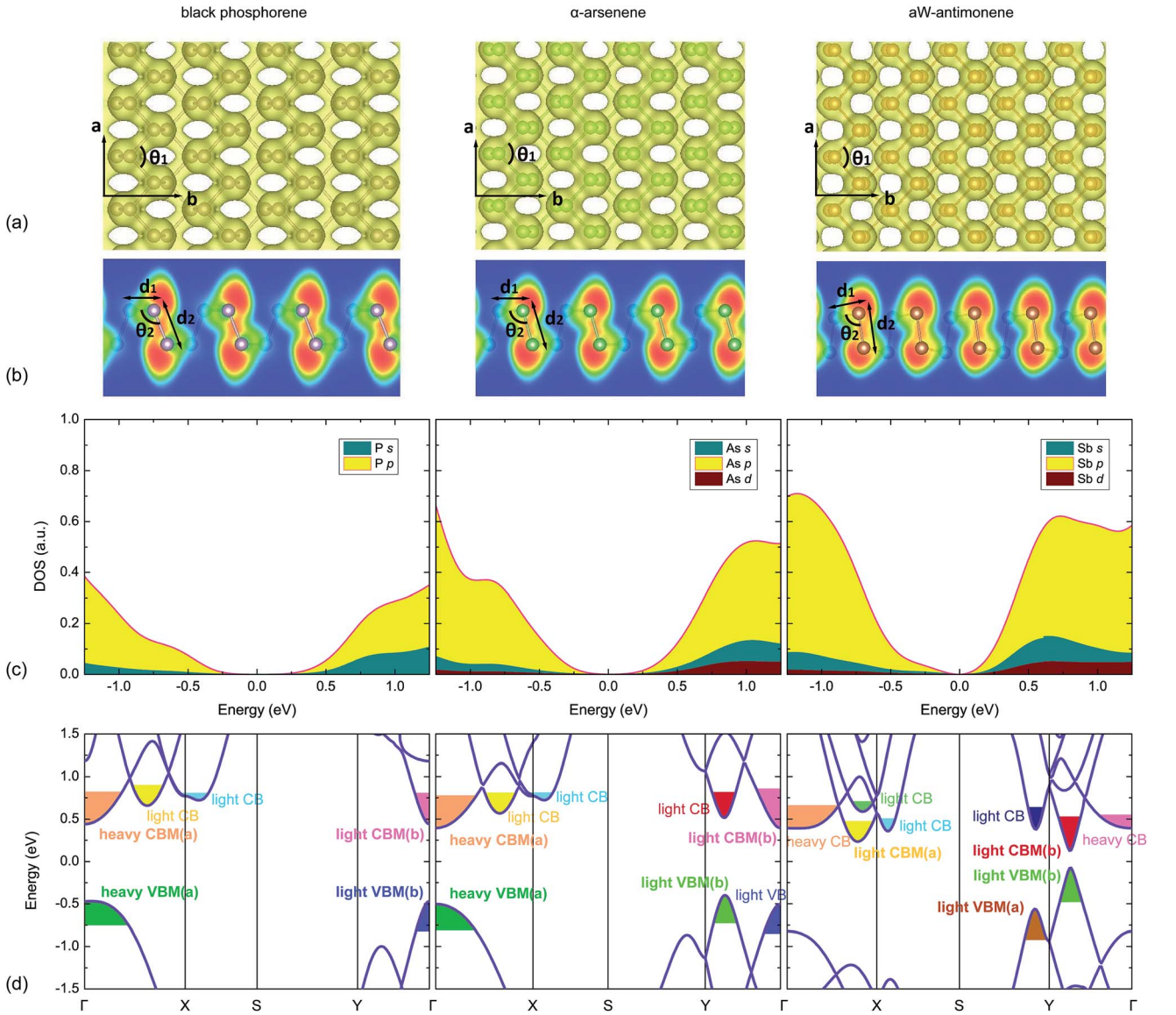

Fig. 2 (a) Top view of the 3D electron localization function of monolayer black phosphorus, α-arsenene and aW-antimonene (isosurface = 0.6), and (b) 2D electron localization function in the plane of d_2 bonds. Increasing electron localization from 0 to 1 is plotted with colors from blue to red. (c) Projected DOS and (d) electronic structure for all studied 2D materials.

Table 1 Optimized geometries and band gaps of all studied 2D group-V materials. Other theoretical data are also presented in parentheses for comparison

	Space group	a (Å)	b (Å)	d_1 (Å)	d_2 (Å)	θ_1 (°)	θ_2 (°)	E_g (eV)
P	*Pmna*	3.30	4.62	2.22	2.26	95.95	104.17	0.91
		(3.32 (ref. 51))	(4.58 (ref. 51))	(2.24 (ref. 51))	(2.28 (ref. 51))	(93.00 (ref. 51))	(103.51 (ref. 51))	(0.91 (ref. 51))
		(3.30 (ref. 72))	(4.64 (ref. 72))					(0.92 (ref. 72))
As	*Pmna*	3.68	4.77	2.51	2.50	94.47	100.66	0.79
		(3.68 (ref. 52))	(4.77 (ref. 52))	(2.50 (ref. 52))	(2.49 (ref. 52))	(94.64 (ref. 52))	(100.80 (ref. 52))	(0.83 (ref. 52))
		(3.71 (ref. 73))	(4.67 (ref. 73))	(2.52 (ref. 73))	(2.51 (ref. 73))	(94.52 (ref. 73))	(100.92 (ref. 73))	
Sb	$Pmn2_1$	4.36	4.73	2.95	2.87	95.31	88.45	0.20
		(4.36 (ref. 42))	(4.74 (ref. 42))	(2.94 (ref. 42))	(2.87 (ref. 42))	(95.3 (ref. 42))		(0.28 (ref. 42))
		(4.28 (ref. 43))	(4.74 (ref. 43))	(2.91 (ref. 43))	(2.84 (ref. 43))			(0.16 (ref. 43))

of 2.22 Å connects the nearest P atoms in the same plane, and the longer d_2 of 2.26 Å connects P atoms between the top and bottom sublayers. Arsenene has a puckered structure as well, but its d_1 is larger than d_2. Different from monolayer black phosphorus and α-arsenene, aW-antimonene has a distorted atomic structure with two sublayers, where atoms in the same sublayer are not in the same planes. This structure is formed due to the asymmetric reconstruction, since the symmetric structure undergoes instability in long-wavelength acoustic vibrations.[43] This reconstruction results in a much larger d_1 than d_2.

Table 1 lists the calculated E_g – consistent with other theoretical studies.[42,43,51,52,72] From P to As and to Sb, the bond length, d, increases with higher atomic number, leading to decreasing orbital overlap. According to eqn (3) and (4), the band gap, E_g, and band width, W, should decrease. This intuition is confirmed by the DOS of monolayer black phosphorus, α-arsenene, and aW-antimonene. As shown in Fig. 2(c), with increasing d, both E_g and W become progressively smaller, while the DOS becomes larger.

As shown in Fig. 2(d), both the valence band maximum (VBM) and the conduction band minimum (CBM) of monolayer black phosphorus occur at the Γ point. The valence band is mainly comprised of P-3p states. A σ bond between two p-orbitals tends to run down from the Γ point, while a π bond runs up.[1] The VBM at the Γ point indicates the dominant σ bonds.

Different from monolayer black phosphorus, α-arsenene is an indirect band gap semiconductor. The VBM occurs at the point along the Γ–Y direction, while the CBM occurs at the Γ point. The energy of the highest valence band along Γ–Y decreases from the Γ point at first and then increases, until reaching the VBM, indicating the weakened σ bonds and strengthened π bonds. With increasing bond length from monolayer black phosphorus to arsenene, the decrease in the orbital overlap weakens the σ bonds, while the p_z–p_z overlapping can be increased by decreased θ_2, as shown in Table 1. This is confirmed by smaller d_2 compared to d_1. The mutual competition between d_1 and d_2 that dictates the VBM can explain, in part, the band structural changes in α-As_xP_{1-x}[77] and strained α-arsenene.[78]

In aW-antimonene, as the bond length further increases, the decrease in the overlap between the p_z orbitals decreases the strength of the π bond and the stability of the planar sublayer cannot be maintained. Through buckling in the sublayer, the decrease in θ_2 results in increasing p_z–p_z overlapping. Thus, its d_2 becomes much smaller than d_1. As a result of the strengthened π bonds, the VBM at the point along the Γ–Y direction significantly exceeds that at the Γ point. A similar trend is observed in the CBM, leading to a direct band gap.

3.2 Bonding structure and carrier mobility

Monolayer black phosphorus, arsenene, and antimonene are non-polar materials, and one advantage of these materials is the absence of strong polar optical phonon scattering. Hereafter, we only consider the acoustic-phonon limited mobility. According to the deformation potential theory,[25,51,79] the carrier mobility can be calculated as

$$\mu^{2D} = \frac{2e\hbar^3 C^{2D}}{3k_B T m^{*2} {E_d}^2}, \quad (5)$$

where e is the electron charge, $\hbar$ is the reduced Planck constant, C^{2D} is the 2D elastic modulus, k_B is the Boltzmann constant, T is the temperature, and E_d is the deformation potential constant. The 2D elastic modulus and the deformation potential constant can be calculated by the total energy and the positions of the CBM and VBM with respect to the lattice dilation up to 1.5%. It should be noted that the method we used is computationally efficient but physically simple. More sophisticated methods based on the Boltzmann transport method with relaxation time approximation can be referred to in some recent studies.[80–85] Table 2 lists the calculated m^*, E_d, and C^{2D}.

The carrier mobilities of monolayer black phosphorus, α-arsenene, and aW-antimonene are strongly influenced by their effective masses. With increasing d, the DOS in Fig. 2(b) becomes larger from P to As and to Sb, which usually implies a higher m^*. However, in part due to the anisotropic structure, complex Fermi surfaces are observed in these materials; hence, a high DOS and a low effective mass can be obtained simultaneously. For monolayer black phosphorus and α-arsenene, the calculated effective masses along the a and b directions are consistent with previous results.[51,73] Although monolayer black phosphorus is a direct band gap semiconductor, its m^* exhibits a strongly anisotropic behavior at the Γ point. For α-arsenene, because of the mutual competition between σ and π bonds, the

Table 2 Predicted effective mass m^*, deformation potential constants E_d, 2D elastic modulus C^{2D}, carrier mobility μ and relaxation time τ of all studied 2D group-V materials

	Direction	Carrier type	m^* (m_0)	E_d (eV)	C^{2D} (J m^{-2})	μ (cm^2 V^{-1} s^{-1})	τ ($\times 10^{-14}$ s)
P	*a*	Hole	6.32	0.05	103.10	13 067.66	4696.50
		Electron	1.19	5.44		34.77	2.36
	b	Hole	0.15	2.82	24.27	2024.38	16.84
		Electron	0.16	1.54		5903.23	52.80
As	*a*	Hole	1.64	1.40	65.23	176.82	16.47
		Electron	1.17	4.13		39.49	2.63
	b	Hole	0.13	8.20	16.86	214.38	1.57
		Electron	0.24	0.76		7224.04	97.95
Sb	*a*	Hole	0.06	9.62	47.03	2145.38	7.07
		Electron	0.21	6.41		358.56	4.34
	b	Hole	0.05	1.19	16.24	76 525.97	201.36
		Electron	0.04	4.20		8093.26	18.51

Fermi surfaces become more complex. Therefore, although the DOS of arsenene is higher than for monolayer black phosphorus, its electron and hole effective masses along the *a* and *b* directions are lower than those for monolayer black phosphorus. As for antimonene, the distorted atomic structure in two sublayers results in a more complex band structure and m^* becomes further lower.

The deformation potential constant, E_d, is defined as the energy change of the VBM and CBM with lattice deformation along the *a* and *b* directions, and reflects the interaction strength of carriers with acoustic phonons.[79,86] A high E_d corresponds to strong electron–phonon coupling. As shown in Fig. 3, the VBM states in black phosphorene and α-arsenene are quite isolated along the *a* direction, and the displacement of phonons causes little change to the energy of these states. Thus, their deformation potential constants are much smaller than those along the *b* direction. Similarly, their deformation potential constants for the CBM states along the *b* direction are smaller than those along the *a* direction. For aW-antimonene, the deformation potential constants are generally larger than those of the other two materials. This anomalous behavior is due to the fact that with a more distorted structure, the bond angles are changed easily in lattice dilation, which significantly changes the orbital overlap.

The anisotropic 2D elastic modulus of these three materials can be attributed to the bonding structure as well. Under uniaxial strain along the *b* direction, the bond angles are more easily changed than those along the *a* direction. In addition, from monolayer black phosphorus to arsenene and to antimonene, the orbital overlap decreases with increasing bond length. Therefore, these systems become "softer". It should be mentioned that weak bond strength implies the slow speed of sound, which, in turn, reduces the lattice thermal conductivity and benefits high thermoelectric performance, as discussed below.

The predicted carrier mobilities for monolayer black phosphorus, arsenene, and antimonene are, in general, moderately high, which agrees well with previous results.[25,51] The anisotropic structure of monolayer black phosphorus normalizes the effect of m^*, E_d, and C^{2D}, leading to generally high hole and electron mobilities along the *a* and *b* directions. The DOS of arsenene is higher than for monolayer black phosphorus. For isotropic materials, a high DOS indicates a heavy m^*. However, benefiting from the anisotropic structure of α-arsenene, the effective masses are generally lower than those of monolayer black phosphorus. For antimonene, the distorted atomic structure of two sublayers results in a more complex band structure, and the number of conduction band minima further increases, as shown in Fig. 2(d). The energy separation of different conduction band minima is 0.1–0.4 eV – comparable to that in PbTe, PbSe, and SnTe.[2] Since the DOS is enhanced by different pockets, a larger DOS and a lower m^* can be obtained at the same time. Thus, a large Seebeck coefficient can be achieved while maintaining a high carrier mobility and the trade-off between S and μ can be overcome.

3.3 Carrier concentration, electrical conductivity, and Seebeck coefficient

One of the main challenges for thermoelectric material design is the trade-off between electrical conductivity and the Seebeck coefficient. Materials with high m^* usually possess large S, but low μ (hence, low σ). Taking advantage of the anisotropic structure, the complex Fermi surfaces in 2D group-V materials can maintain the band shape (small m^*) and enhance the DOS (large S) at the same time. Thus, the optimization of electrical transport properties can be realized using intrinsic material properties.

σ and S at temperature, T, and Fermi level, E_F, can be calculated within the Boltzmann transport theory.[16] To determine the electrical transport properties under doping, we use the rigid band approximation, which assumes that the electronic structure is unchanged with doping and only the Fermi level, E_F, is shifted. This approximation has described the thermoelectric properties of many 2D materials accurately.[87,88] A negative E_F represents p-type doping, while a positive E_F represents n-type doping.

The carrier concentration under doping can be calculated using an integral over the Brillouin zone for holes or electrons with energy, ε,[89,90]

$$n_h = \frac{2}{S}\iint_{BZ}[1 - f_0(T, \varepsilon, E_F)]D(\varepsilon)d\varepsilon, \quad (6)$$

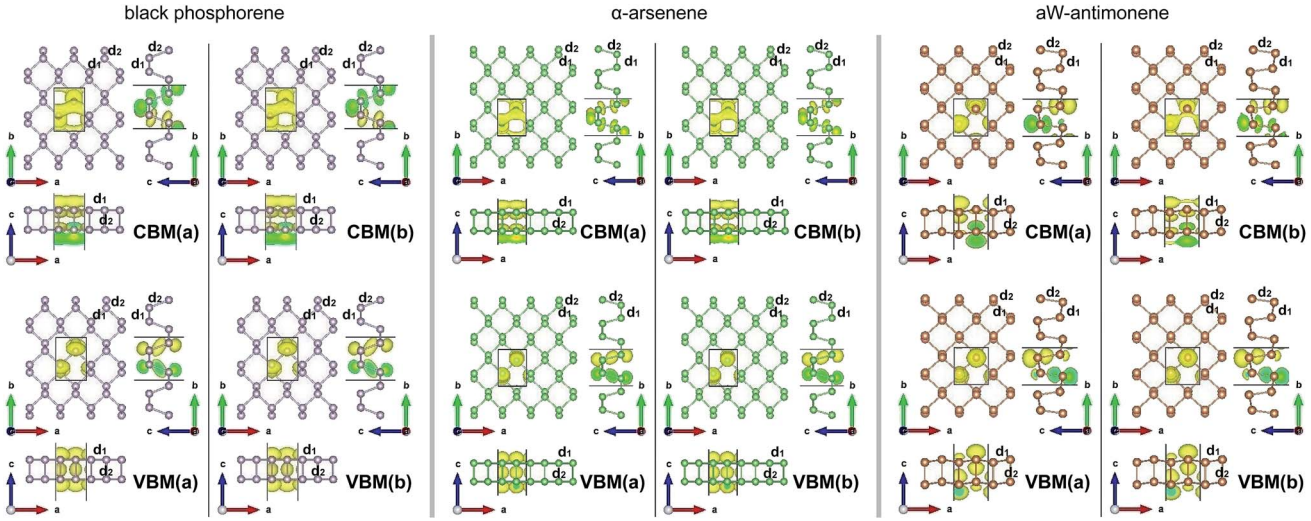

Fig. 3 Charge density of the CBM and VBM states (isosurface = 0.004) along the *a* and *b* directions for all studied 2D materials.

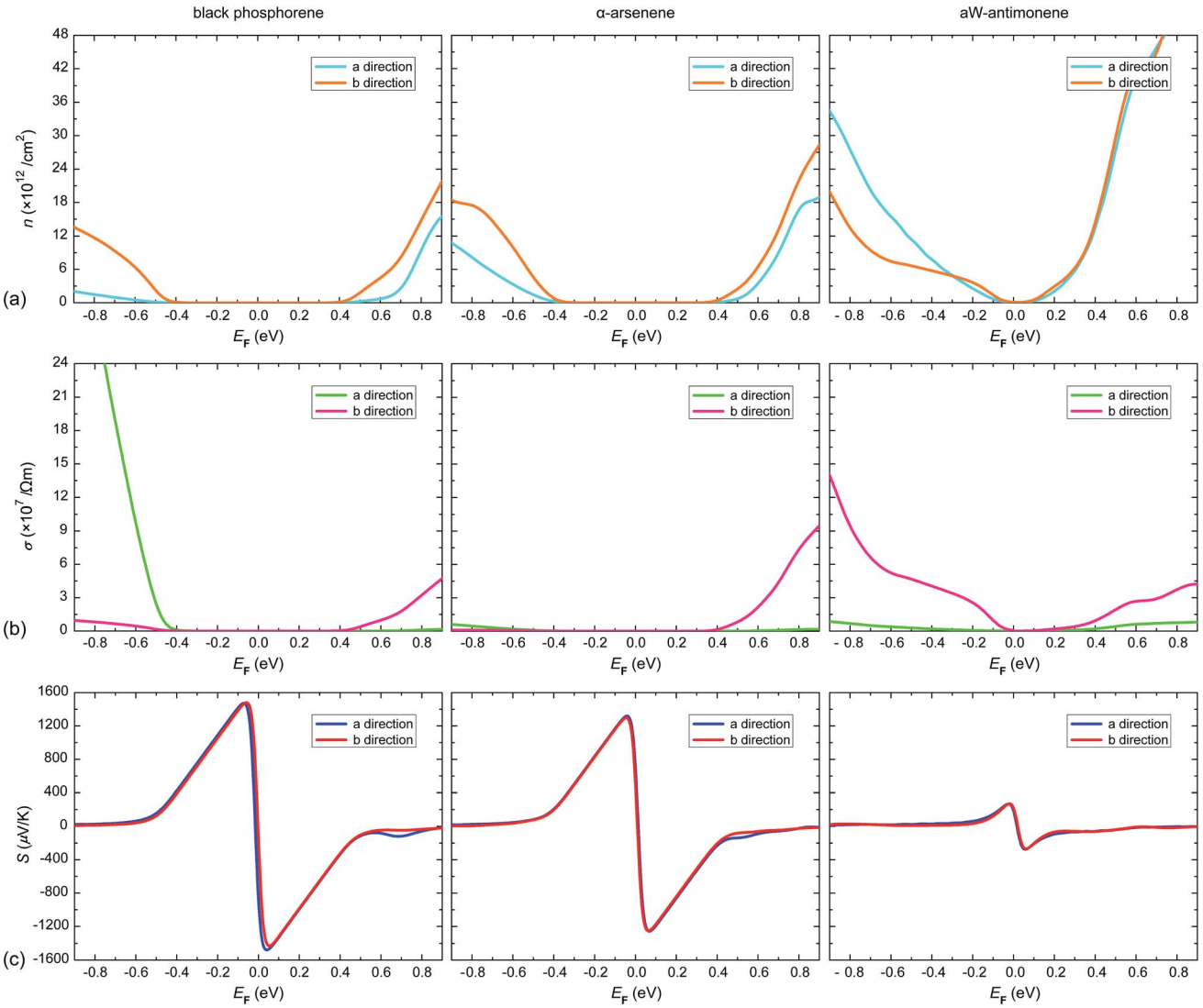

Fig. 4 (a) Calculated carrier concentration, (b) electrical conductivity and (c) Seebeck coefficient as a function of chemical potential at 300 K.

$$n_e = \frac{2}{S}\iint_{BZ} f_0(T,\varepsilon,E_F)D(\varepsilon)d\varepsilon, \quad (7)$$

where S is the area of a 2D unit cell, $f_0(T,\varepsilon,E_F)$ is the Fermi–Dirac distribution function at temperature, T, and Fermi level, E_F, and $D(\varepsilon)$ is the DOS. Fig. 4(a) plots the relationship between E_F and the corresponding carrier concentration for both p-type and n-type doping. From monolayer black phosphorus to arsenene and to antimonene, the carrier concentration n increases with increasing DOS [Fig. 2(c)].

Using the Boltzmann transport theory for electrons,[16] a ratio σ/τ that increases with increasing n can be obtained. The electrical conductivity, σ, can be estimated with the given carrier relaxation time, τ. According to $\mu = e\tau/m^*$, a large τ can be achieved with increasing μ and increasing m^*, as shown in Table 2. Fig. 4(b) shows the calculated σ. For holes in monolayer black phosphorus, τ along the a direction is much longer than along the b direction. Thus, although n along the a direction is lower than that along the b direction, its σ is much higher. Similarly, in α-arsenene, the τ of electrons along the b direction is the highest, leading to the highest σ. In aW-antimonene, the carrier relaxation times along the b direction are much higher than those along the a direction, which results in higher electrical conductivities along the b direction for both holes and electrons.

To investigate the ability to produce voltage under a temperature difference in a circuit, we calculated the Seebeck coefficient, S, as a function of E_F, as shown in Fig. 4(c). For a degenerate semiconductor with parabolic band dispersion, S can be understood by the Mott relation[2,91]

$$S = \frac{2{k_B}^2 T}{3e\hbar^2} m^* \left(\frac{\pi}{3n}\right)^{2/3}. \quad (8)$$

According to the Mott relation, S is larger at the edge of heavier band m^* or at low carrier concentration, n. With generally higher m^*, monolayer black phosphorus and arsenene have much larger S than antimonene. In addition, S usually reaches a peak value at small E_F, corresponding to low carrier concentration. Antimonene has a much higher carrier concentration even at small E_F, which leads to a smaller S as well. However, a high carrier concentration also has one advantage: a high σ. Compared with monolayer SnSe, although the peak value of S in antimonene is about one order of magnitude smaller, its σ along the b direction is enhanced by nearly one order of magnitude.[92] Actually, although smaller than that of monolayer black phosphorus and arsenene, a good Seebeck coefficient of 270 $\mu V\ K^{-1}$ can be obtained in antimonene, due to the band convergence effect, – comparable to those for few-layer and bulk MoS_2.[93,94] Therefore, high thermoelectric performance could still be expected in aW-antimonene.

4 Chemical bonding and phonon transport

A low thermal conductivity is essential to obtain a high thermoelectric performance. The thermal conductivity by electrons κ_{el} relates to the electrical conductivity σ *via* the Wiedemann–Franz law,

$$\kappa_{el} = L\sigma T, \quad (9)$$

where L is the Lorenz number and can be derived from the calculated Seebeck coefficients.[95–97] Here, we focus on reducing the lattice thermal conductivity, κ_L, by understanding the role of chemical bonds in phonon transport, which provides a simple, intuitive insight into the search for low lattice thermal conductivity materials.

The in-plane lattice thermal conductivity, κ_L, can be calculated as[17]

$$\kappa_L(\alpha) = \frac{1}{abh_v}\sum_{\lambda} C_\lambda {v_{\lambda\alpha}}^2 \tau_{\lambda\alpha}, \quad (10)$$

where h_v is the interlayer distance,[66] C_λ is the specific heat per mode, $v_{\lambda\alpha}$ is the group velocity, and $\tau_{\lambda\alpha}$ is the relaxation time of mode λ along the α direction. At room temperature, the specific heat of the system becomes 83.81 J mol^{-1} K^{-1}, 67.70 J mol^{-1} K^{-1}, and 60.90 J mol^{-1} K^{-1}, respectively, for monolayer black phosphorus, arsenene and antimonene, approaching the Dulong–Petit classical limit (99.77 J mol^{-1} K^{-1}). Hereafter, the phonon transport properties, such as phonon velocities and phonon scattering rates, are discussed in relation to the chemical bonding. The bonding strength determines the phonon sound velocities. The phonon scattering rate – the inverse of relaxation time – is strongly influenced by bond anharmonicity. In fact, the anisotropic structure can suppress phonon transport as effectively as the defect or adatom engineering.

4.1 Bonding strength and phonon velocity

The bonding strength determines the speed of phonons. This dependence can be understood by a simplified picture as atoms with mass, M, connected by bonds with spring constant, K. The speed of phonons is given by $v \sim \sqrt{K/M}$.[1] Here, the anisotropic structures of monolayer black phosphorus, arsenene, and antimonene result in anisotropic bonding strength; hence, anisotropic sound velocities of longitudinal acoustic phonons inhibit heat propagation in the low-phonon-velocity direction.

Fig. 5(a) shows the calculated phonon dispersion of monolayer black phosphorus, arsenene, and antimonene. The lowest ZA branch is quadratic near the Γ point, due to low lattice dimensionality.[98] Compared to buckled 2D group-V structures, such as blue phosphorene, β-arsenene, and β-antimonene[66,99] monolayer black phosphorus, α-arsenene, and aW-antimonene have two more atoms in the unit cell, indicating more phonon branches. Intuitively, more atoms indicate more complex structures, making the transport path more tortuous for phonons. The physical insight is increasing the number of atoms per unit cell leads to more phonon branches and creates more scattering opportunities for phonons, ultimately reducing κ_L.[36]

As shown in Table 3, the highest phonon frequency decreases from P to As and to Sb. In a monoatomic linear chain model, the scale of the phonon branch is dominated by the bonding strength and the atomic mass. The largest harmonic interatomic force constant, Φ, and mass density, ρ, of all studied 2D materials are shown in Table 3. There is a clear decrease in Φ and increase in ρ down the columns, leading to

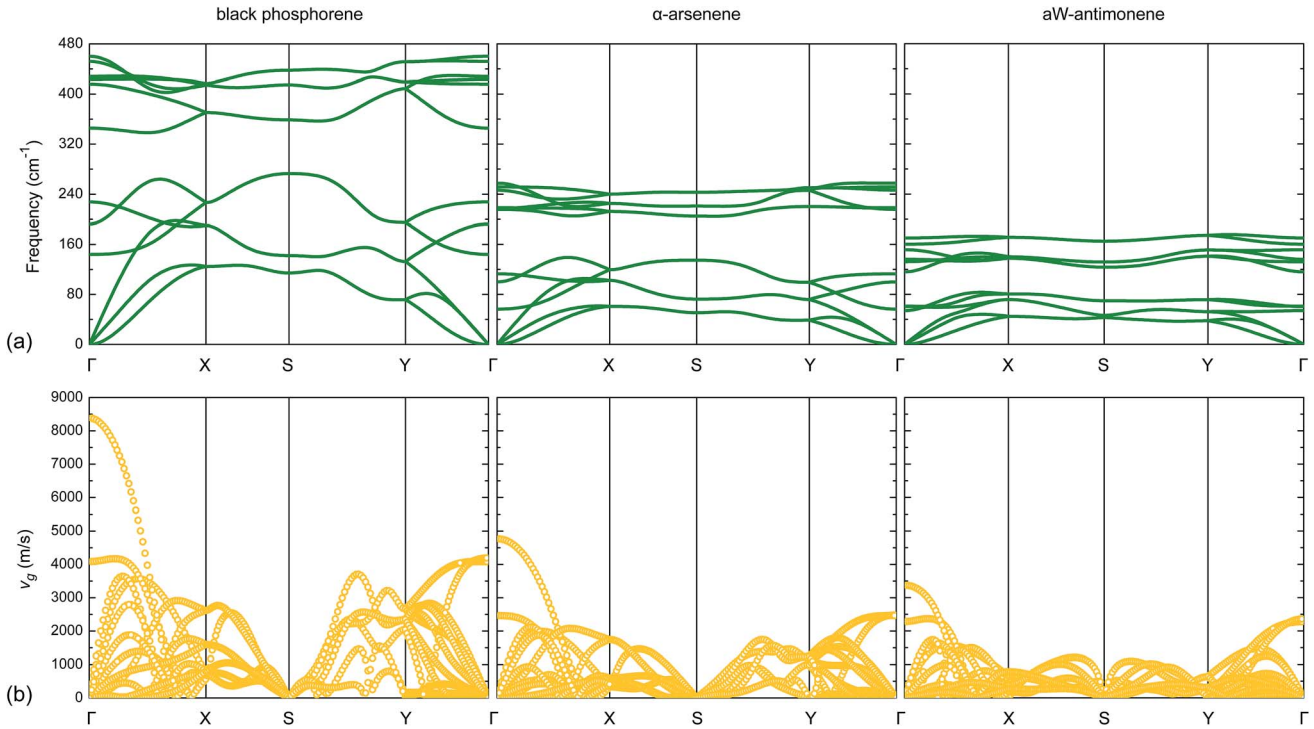

Fig. 5 Calculated (a) phonon dispersion and (b) group velocities for all studied 2D materials.

Table 3 Calculated highest phonon frequency ω, largest harmonic interatomic force constant Φ, mass density ρ, 2D elastic coefficients C_{ij}^{2D} of all studied 2D materials

	ω (cm^{-1})	Φ (eV Å^{-2})	ρ (mg m^{-2})	C_{11}^{2D} (J m^{-2})	C_{12}^{2D} (J m^{-2})	C_{22}^{2D} (J m^{-2})	C_{66}^{2D} (J m^{-2})
P	460.25	12.44	1.35	103.10	16.93	24.29	22.64
As	257.78	8.19	2.84	65.23	19.25	16.69	17.04
Sb	175.49	4.81	3.93	47.03	13.15	16.25	22.38

decreasing phonon frequency, which further reduces the speed of phonons.

To understand quantitatively the dependence of the speed of phonons on the strength of chemical bonding, we calculate the elastic tensor coefficients, including ionic relaxations using the finite difference method.[100,101] The 2D coefficients, C_{ij}^{2D}, are renormalized by the vacuum space between the 2D layers,[102] *i.e.*, $C_{ij}^{2D} = cC_{ij}^{3D}$. Table 3 lists the calculated C_{ij}^{2D}.

The speed of phonons propagating through the lattice can be estimated by the speed of sound,[1]

$$v_s(\mathrm{LA})_{a/b} = \sqrt{\frac{C_{11/22}^{2D}}{\rho}}, \quad (11)$$

$$v_s(\mathrm{TA}) = \sqrt{\frac{C_{12}^{2D}}{\rho}}. \quad (12)$$

The calculated sound velocities are shown in Table 4. We also compare the phonon group velocities for the TA and LA modes in the long-wavelength limit, which agree well with the sound velocities. The sound velocities for the LA branch manifest significant anisotropy, due to anisotropic bonding strength. The strength along the *a* direction is much higher than that along the *b* direction, which can be understood by the bonding structure. Under uniaxial strain along the *b* direction, the bond angles are more easily changed than those along the *a* direction. Thus, in the *b* directions, the speed of the phonons tends to be low, which inhibits heat propagation.

The Debye temperature, Θ_D, can be calculated from the average sound velocity v_s[103]

$$\Theta_D = \frac{hv_s}{k_B}\left(\frac{4\pi N}{S}\right)^{1/2}, \quad (13)$$

where N is the number of atoms in the cell. Table 4 shows the calculated Θ_D. When the temperature is above Θ_D, all phonon modes are excited.[104] Thus, a low Θ_D indicates a strong three-phonon scattering and, therefore, low κ_L. It could be expected that κ_L decreases from P to As and to Sb, and κ_L along the *a* direction is higher than that along the *b* direction.

Table 4 Calculated sound velocities v_s, phonon group velocities v_g in the long-wavelength limit and Debye temperature Θ_D of all studied 2D group-V materials along the *a* and *b* directions

	Direction	v_s (LA) (m s^{-1})	v_g (LA) (m s^{-1})	v_s (TA) (m s^{-1})	v_g (TA) (m s^{-1})	Θ_D (K)
P	*a*	8740	8380	3540	4080	644
	b	4240	4190	3540	4080	533
As	*a*	4790	4770	2610	2460	419
	b	2430	2480	2610	2460	325
Sb	*a*	3380	3370	1830	2280	272
	b	2030	2360	1830	2280	230

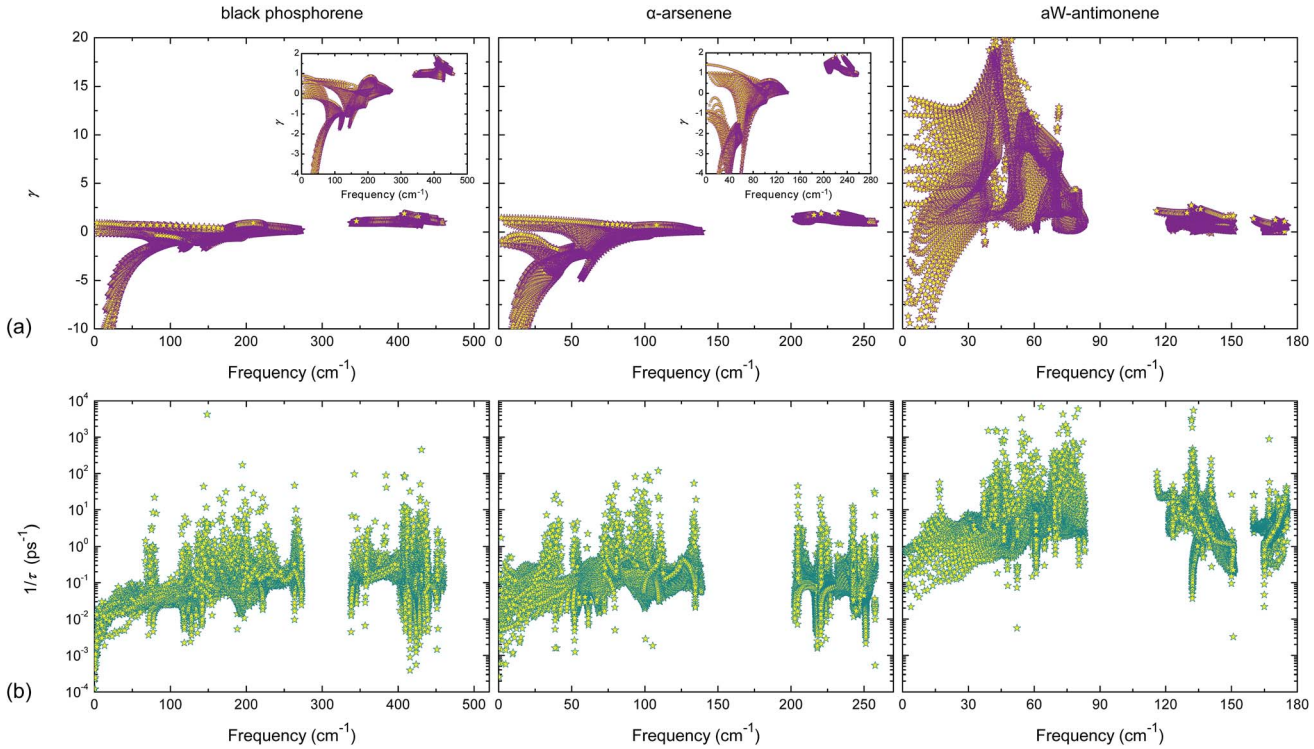

Fig. 6 Calculated (a) mode Grüneisen parameters and (b) phonon scattering rates at 300 K for all studied 2D materials.

4.2 Bond anharmonicity and phonon interaction

A lattice with harmonic vibrations has infinite lattice thermal conductivity, because harmonic phonons have no chance to scatter from each other. Phonon scattering is determined by the anharmonicity of the chemical bond.[105] In chemical terms, bond anharmonicity measures the asymmetry in vibration. Anharmonicity can be characterized by the mode Grüneisen parameters. The larger the mode Grüneisen parameters, the stronger the anharmonicity, the more frequently a phonon becomes scattered by other phonons.

Fig. 6(a) shows the calculated mode Grüneisen parameters. Materials with increasing size and mass usually have larger Grüneisen parameters.[1] Therefore, the mode Grüneisen parameters for monolayer black phosphorus are slightly smaller than those for α-arsenene. Interestingly, aW-antimonene not only shows higher mode Grüneisen parameters than monolayer black phosphorus and arsenene, but even larger than most state-of-the-art thermoelectric materials, such as PbTe, SnTe and SnSe.[106,107]

The origin of the strong bond anharmonicity in antimonene can be traced to the structural distortion. The asymmetric reconstruction in antimonene is sensitive to local distortions induced by phonons.[108] When the bond is compressed and stretched, the change in the electron configuration is highly asymmetric, which results in a strong bond anharmonicity.[109] In addition, the Sb lone pair tends to manifest structural asymmetry and further increases anharmonicity in the lattice,[110–112] leading to the anomalously large Grüneisen parameters in aW-antimonene.

The Grüneisen parameters reflect the strength of phonon scattering. Fig. 6(b) shows the calculated phonon scattering rates of monolayer black phosphorus, arsenene, and antimonene at 300 K. The phonon scattering rates for arsenene are moderately higher than those for monolayer black phosphorus because of slightly larger Grüneisen parameters. In aW-antimonene, the phonon scattering rates are strongly enhanced with much larger Grüneisen parameters.

In addition to bond anharmonicity, phonon scattering also depends on the number of channels available for a phonon to become scattered (whether a three-phonon group satisfies the energy and quasi-momentum conservation) – determined by the phonon dispersion directly. In fact, comparing the phonon dispersion of our materials with buckled group-V monolayers can provide an intuition for their phonon scattering behavior. Different from their buckled counterparts, such as blue phosphorene,[39] there is no acoustic-optical gap in our 2D group-V materials, providing more channels for acoustic phonons to be scattered into optical phonons. Thus, the phonon scattering rates in our anisotropic 2D group-V materials are much higher than those of their buckled counterparts, especially for aW-antimonene.[99]

4.3 Lattice thermal conductivity

The traditional routes to improve zT by suppressing lattice thermal conductivity include introduction of lattice imperfections,[6,113] nanostructuring,[114] mesoscale structuring,[115] and even all-scale hierarchical architectures.[116,117] Finding materials with intrinsically low thermal conductivity can avoid these complex approaches to reduce thermal conductivity. Intrinsically low thermal conductivity may arise from strong bond anharmonicity, anisotropic bond structure, a complex crystal, and lone-pair electrons,[2] as shown in the case of our 2D group-V materials.

Fig. 7 shows the temperature dependence of lattice thermal conductivity for monolayer black phosphorus, arsenene, and antimonene. κ_L exhibits strong anisotropic behavior. Table 5 presents κ_L along the a and b directions at 300 K. The calculated thermal conductivities of monolayer black phosphorus and α-arsenene are in good agreement with most previous results.[63,64,66,68–71,118,119] Noticeably, Qin *et al.* have reported a lower κ_L for monolayer black phosphorus,[65,120] which might further improve its thermoelectric performance. For aW-antimonene, our κ_L is more than one order of magnitude lower than that reported in previous work.[66] This is probably due to linear ZA dispersion in previous work, which comes from the violation of some invariance conditions in 2D materials because of imperfect computational algorithms.[98]

Table 5 Calculated lattice thermal conductivity κ_L along the a and b directions at 300 K, and contribution of ZA, TA, LA and all optical phonons (O) towards κ_L for all studied 2D materials

	Direction	κ_L (W mK^{-1})	ZA (%)	TA (%)	LA (%)	O (%)
P	a	126.70	27.58	23.78	35.13	13.51
	b	35.02	17.41	19.28	37.57	25.74
As	a	28.10	15.59	13.97	45.97	24.47
	b	4.25	4.71	12.89	41.20	41.20
Sb	a	0.36	7.19	8.22	71.46	13.13
	b	0.18	11.20	17.70	60.11	10.98

Most excitingly, due to the anisotropic structure of all studied 2D group-V materials, κ_L along the a direction is higher than that along the b direction. A thermal conductivity anisotropy ratio of 3.6, 6.6 and 2.0 is obtained, respectively, for monolayer black phosphorus, arsenene and antimonene. This anisotropy makes these materials promising for orientation-controlled thermal management. Generally, the a transport direction with higher κ_L is preferred in nanoelectronics, while the b direction is preferred in thermoelectric devices. For monolayer black phosphorus, κ_L along the a direction is comparable to that for the perfect monolayer MoS_2 using the same approach,[121,122] indicating efficient heat dissipation; along the b direction, κ_L is even lower than that of highly defective MoS_2 with a vacancy concentration of 7.4%.[122] Thus, compared with reducing κ_L by introducing lattice imperfections, anisotropic materials have intrinsic potential to suppress phonon transport by a simple in-plane orientation. For α-arsenene, κ_L along the a direction is similar to that for low-buckled silicene (28.3 W mK^{-1}).[123] As noted in our previous study, by adding Si adatoms, the κ_L of silicene can be reduced to 2.86 W mK^{-1} after the dumbbell structure is formed.[36] Here, we show that the anisotropic structure in arsenene can suppress heat transport as effectively as adatom engineering.

It is also worth noting that aW-antimonene exhibits a lower lattice thermal conductivity for both the a and b directions – even lower than those for high performance thermoelectric materials, for instance, 2.0–2.5 W mK^{-1} at 300 K in monolayer SnSe.[92] This extraordinarily low κ_L can be attributed to weak bonding strength and strong bond anharmonicity, which result

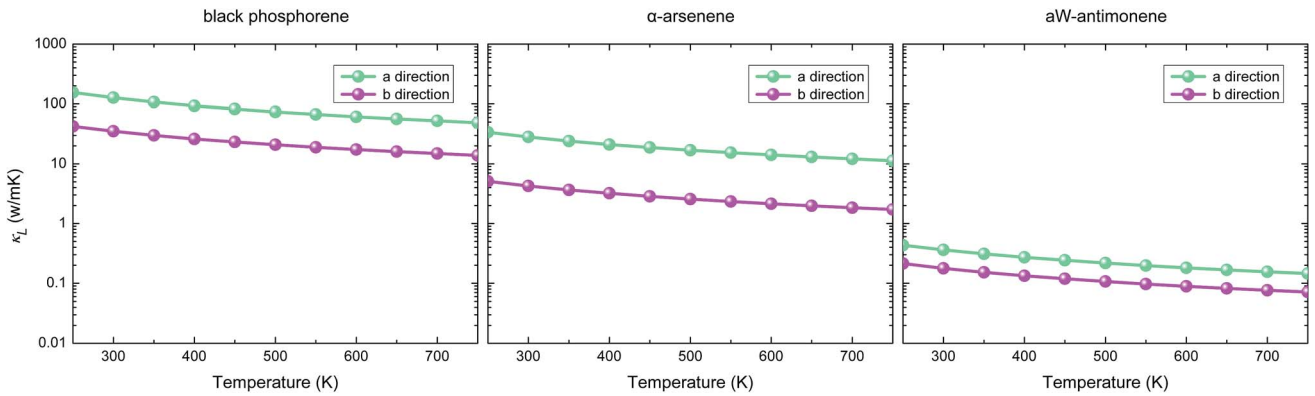

Fig. 7 Lattice thermal conductivity for all studied 2D materials as a function of temperature.

in low phonon velocities and high phonon scattering rates, respectively. In addition, the Sb lone pair electrons might also play a role in reducing κ_L.

5 Thermoelectric performance

The thermoelectric performance is the competition between electrical and thermal transport. Using all the transport coefficients, we obtain the thermoelectric figure of merit as a function of chemical potential at 300 K for monolayer black phosphorus, α-arsenene, and aW-antimonene in Fig. 8. In general, the maximum zT values are observed near the edge of the VBM or the CBM, as shown in Table 6. The highest thermoelectric performance for our materials is comparable to that for monolayer SnSe,[92] graphene nanoribbons,[124] and graphyne (sheets,[125–127] nanoribbons[128–131] and nanotubes[132]) calculated by similar approaches, making them promising candidates for room temperature thermoelectric materials. With elevated temperature, it can be expected that zT values would be further improved, due to decreasing κ_L as shown in Fig. 7, because the phonon scattering becomes stronger. Fig. 8 also presents the calculated thermoelectric figure of merit zT at 500 K and 700 K. For black phosphorus and α-arsenene, the zT curve becomes higher with increasing temperature in a wide doping range, indicating higher thermoelectric performance.

We also list the corresponding transport coefficients for more insights. For monolayer black phosphorus, the maximum zT for p-type doping along the a direction benefits from its ultrahigh carrier mobility, 13 067.66 $cm^2\ V^{-1}\ s^{-1}$, and good Seebeck coefficient, 236.51 $\mu V\ K^{-1}$, which result in a high thermoelectric power factor – 513.50 $mW\ mK^{-2}$. In the b direction, a good zT is obtained for both electrons and holes. This can be attributed to the anisotropic structure that helps to overcome the trade-off between S and σ, and suppresses the lattice thermal conductivity along the b direction. For arsenene, a high thermoelectric performance for n-type doping along the b direction is achieved due to the small deformation potential, large Seebeck coefficient and low lattice thermal conductivity. It should also be noted that, in non-degenerate semiconductors, both electrons and phonons contribute largely to the total thermal conductivity, κ.

Although the peak value of S in antimonene is nearly one order of magnitude smaller than those for monolayer black phosphorus and arsenene, its peaks in zT are highest because of its relatively large Seebeck coefficient and ultralow lattice thermal conductivity. The complex crystal structure in aW-

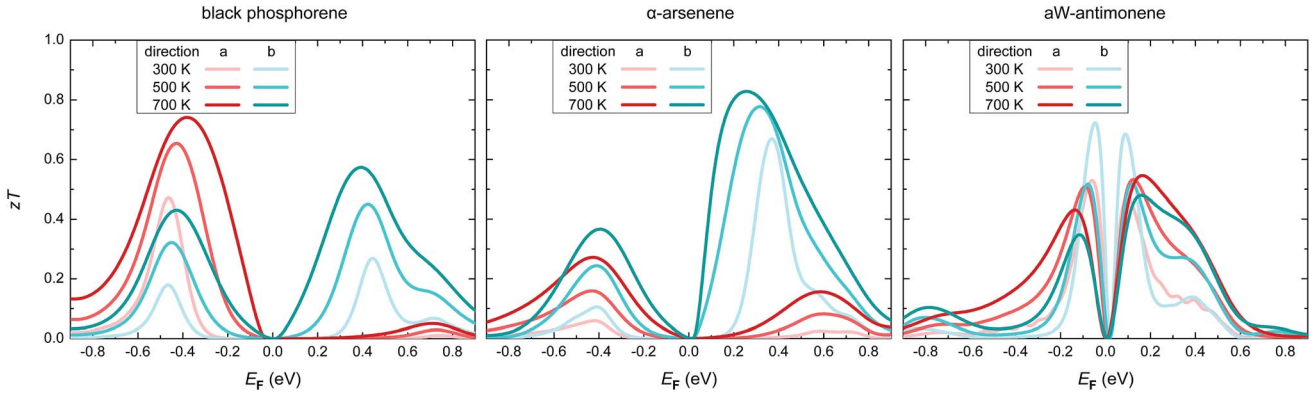

Fig. 8 Calculated thermoelectric figure of merit for all studied 2D materials at 300 K, 500 K, and 700 K.

Table 6 Maximum zT values with their position E_F for both p-type and n-type doping along the a and b directions at 300 K of all studied 2D materials. The corresponding carrier concentration n, electrical conductivity σ, Seebeck coefficient S, total thermal conductivity κ, and electronic thermal conductivity κ_{el} are also listed for comparison

	Direction	Carrier type	E_F (eV)	zT	σ (/μΩ m)	S ($\mu V\ K^{-1}$)	κ ($W\ mK^{-1}$)	κ_{el} ($W\ mK^{-1}$)
P	a	Hole	−0.46	0.47	9.18	236.51	326.74	200.05
		Electron	0.74	0.01	0.52	−97.28	131.40	4.71
	b	Hole	−0.47	0.18	0.76	191.01	46.64	11.62
		Electron	0.44	0.27	1.16	−206.34	55.22	20.20
As	a	Hole	−0.42	0.06	0.23	164.87	31.21	3.12
		Electron	0.70	0.02	0.78	−57.47	34.39	6.30
	b	Hole	−0.41	0.11	0.06	176.35	5.10	0.85
		Electron	0.37	0.67	0.58	−285.68	21.21	16.96
Sb	a	Hole	−0.06	0.53	0.06	216.81	1.65	1.29
		Electron	0.10	0.47	0.04	−216.36	1.26	0.90
	b	Hole	−0.04	0.72	2.42	235.77	55.76	55.58
		Electron	0.09	0.69	0.22	−234.39	5.38	5.20

antimonene leads to a complex Fermi surface to achieve a large S, while maintaining a high μ due to the small effective mass. S usually reaches a peak value at small E_F, while σ increases with E_F. Therefore, the high zT also benefits from a small band gap, one of the main reasons for choosing anisotropic 2D group-V materials using a chemical picture of bond-orbital theory. Moreover, a decrease in lattice thermal conductivity in antimonene can be expected because of the weak interatomic bonding and large atomic mass from a chemical point of view. In addition, its asymmetric structure and Sb lone pair result in strong anharmonicity, which further reduces κ_L.

6 Conclusion

We discuss chemical intuition in the search to find high performance thermoelectric materials. A simple understanding of how chemical bonds affect the electrical and thermal transport properties provides new strategies for identifying 2D materials with intrinsically high thermoelectric performance. Three anisotropic group-V materials, monolayer black phosphorus, α-arsenene and aW-antimonene, are chosen for exploration by using a simplified bonding model.

The electrical transport properties depend on the structural chemistry, such as bond length and bonding structure. The increasing bond length from P to As and to Sb implies a decreasing band gap and larger DOS, which further affect the thermoelectric transport properties. The bonding structure can explain the anisotropically high carrier mobilities in these materials. In addition, the anisotropic crystal structure gives rise to a complex Fermi surface, especially for aW-antimonene with asymmetric distortion. As a result, a low effective mass (high electrical conductivity) and a large DOS (large Seebeck coefficient) can be obtained at the same time. Thus, the trade-off between σ and S is overcome.

The phonon transport properties are linked to concepts, such as bonding strength and bond anharmonicity. Due to the anisotropic bonding strength, the phonon velocities tend to be low along the b direction, inhibiting heat propagation. The strong bond anharmonicity coming from the asymmetric structure of antimonene strongly enhances phonon scattering. Therefore, the lattice thermal conductivity of aW-antimonene is lower than those for state-of-the-art thermoelectric materials. The anisotropic thermal conductivity creates new opportunities for thermal management as well.

Because of these intrinsic transport properties, monolayer black phosphorus, α-arsenene, and aW-antimonene are predicted to be promising candidates to realize high thermoelectric performance. Our chemically intuitive approach provides a simple, but effective, framework to identify new thermoelectric materials and evaluate their electrical and phonon transport properties.

6.1 Computational details

First principles calculations are performed using the Vienna *ab initio* simulation package (VASP) based on density functional theory (DFT).[133] The generalized gradient approximation (GGA) in the Perdew–Burke–Ernzerhof (PBE) parameterization for the exchange–correlation functional is used. A plane-wave basis set is employed with a kinetic energy cutoff of 600 eV. We use the projector-augmented-wave (PAW) potential. A 21 × 21 × 1 q-mesh is used during structural relaxation for the unit cell until the energy differences are converged within 10^{-6} eV, with a Hellmann–Feynman force convergence threshold of 10^{-4} eV Å^{-1}. We maintain an interlayer vacuum spacing larger than 20 Å to eliminate interactions between adjacent layers.

The electrical transport properties are obtained using semi-classical Boltzmann transport theory and the rigid band approach as implemented in the BoltzTraP code.[16,89] The constant relaxation time approximation is employed, which is valid when the relaxation time does not vary strongly with the energy scale of k_BT.[87,134] A dense 51 × 51 × 1 q-mesh is introduced to enable accurate Fourier interpolation of the Kohn–Sham eigenvalues. The initial k-mesh is interpolated to a mesh 50 times denser than the original.

The in-plane κ can be calculated iteratively using the ShengBTE code as a sum of contributions for all the phonon modes.[17,135–138] The harmonic interatomic force constants (IFCs) are obtained by density functional perturbation theory (DFPT) using a 5 × 5 × 1 supercell with a 5 × 5 × 1 q-mesh.[139] The anharmonic IFCs are calculated using a supercell-based, finite-difference method,[137] and a 3 × 4 × 1 supercell with a 5 × 5 × 1 q-mesh is used. We include the interactions with the eight nearest-neighbor atoms. A discretization of the Brillouin zone (BZ) into a Γ-centered regular grid of 91 × 91 × 1 q points is introduced with the scale parameter for broadening chosen as 1.

Conflicts of interest

There are no conflicts to declare.

Acknowledgements

We acknowledge helpful discussions with Dr Jesés Carrete Montaña from TU Wien and Prof. Natalio Mingo from CEA-Grenoble. This work is supported by the National Natural Science Foundation of China under Grant No. 11374063 and 11404348, and the National Basic Research Program of China (973 Program) under Grant No. 2013CBA01505. Work at Ames Laboratory is partially supported by the U.S. Department of Energy, Office of Basic Energy Science, Division of Materials Science and Engineering (Ames Laboratory is operated for the U.S. Department of Energy by Iowa State University under Contract No. DE-AC02-07CH11358). The European Research Council under ERC Advanced Grant No. 320081 (PHOTOMETA) supports work at FORTH.

References

1 W. G. Zeier, A. Zevalkink, Z. M. Gibbs, G. Hautier, M. G. Kanatzidis and G. J. Snyder, *Angew. Chem., Int. Ed.*, 2016, **55**, 6826–6841.
2 G. Tan, L.-D. Zhao and M. G. Kanatzidis, *Chem. Rev.*, 2016, **116**, 12123–12149.

3 A. Mehdizadeh Dehkordi, M. Zebarjadi, J. He and T. M. Tritt, *Mater. Sci. Eng., R*, 2015, **97**, 1–22.
4 J. Yang, L. Xi, W. Qiu, L. Wu, X. Shi, L. Chen, J. Yang, W. Zhang, C. Uher and D. J. Singh, *npj Comput. Mater.*, 2016, **2**, 15015.
5 Y.-L. Pei, H. Wu, D. Wu, F. Zheng and J. He, *J. Am. Chem. Soc.*, 2014, **136**, 13902–13908.
6 G. Tan, F. Shi, S. Hao, H. Chi, L.-D. Zhao, C. Uher, C. Wolverton, V. P. Dravid and M. G. Kanatzidis, *J. Am. Chem. Soc.*, 2015, **137**, 5100–5112.
7 S. I. Kim, K. H. Lee, H. A. Mun, H. S. Kim, S. W. Hwang, J. W. Roh, D. J. Yang, W. H. Shin, X. S. Li, Y. H. Lee, G. J. Snyder and S. W. Kim, *Science*, 2015, **348**, 109.
8 Z. Li, C. Xiao, H. Zhu and Y. Xie, *J. Am. Chem. Soc.*, 2016, **138**, 14810–14819.
9 B. C. Sales, D. Mandrus, B. C. Chakoumakos, V. Keppens and J. R. Thompson, *Phys. Rev. B: Condens. Matter Mater. Phys.*, 1997, **56**, 15081–15089.
10 H. Lin, G. Tan, J.-N. Shen, S. Hao, L.-M. Wu, N. Calta, C. Malliakas, S. Wang, C. Uher, C. Wolverton and M. G. Kanatzidis, *Angew. Chem., Int. Ed.*, 2016, **55**, 11431–11436.
11 L.-D. Zhao, G. Tan, S. Hao, J. He, Y. Pei, H. Chi, H. Wang, S. Gong, H. Xu, V. P. Dravid, C. Uher, G. J. Snyder, C. Wolverton and M. G. Kanatzidis, *Science*, 2016, **351**, 141.
12 J. He, M. Amsler, Y. Xia, S. S. Naghavi, V. I. Hegde, S. Hao, S. Goedecker, V. Ozoliņš and C. Wolverton, *Phys. Rev. Lett.*, 2016, **117**, 046602.
13 W. Chen, J.-H. Pohls, G. Hautier, D. Broberg, S. Bajaj, U. Aydemir, Z. M. Gibbs, H. Zhu, M. Asta, G. J. Snyder, B. Meredig, M. A. White, K. Persson and A. Jain, *J. Mater. Chem. C*, 2016, **4**, 4414–4426.
14 A. Faghaninia, G. Yu, U. Aydemir, M. Wood, W. Chen, G.-M. Rignanese, G. J. Snyder, G. Hautier and A. Jain, *Phys. Chem. Chem. Phys.*, 2017, **19**, 6743–6756.
15 F. Zhou, W. Nielson, Y. Xia and V. Ozoliņš, *Phys. Rev. Lett.*, 2014, **113**, 185501.
16 G. K. Madsen and D. J. Singh, *Comput. Phys. Commun.*, 2006, **175**, 67–71.
17 W. Li, J. Carrete, N. A. Katcho and N. Mingo, *Comput. Phys. Commun.*, 2014, **185**, 1747–1758.
18 W. A. Harrison, *Electronic structure and the properties of solids: the physics of the chemical bond[M]*, Courier Corporation, 2012.
19 T. Koopmans, *Physica*, 1934, **1**, 104–113.
20 W. A. Harrison, *Pure Appl. Chem.*, 2009, **61**, 2161.
21 G. D. Mahan, *J. Appl. Phys.*, 1989, **65**, 1578–1583.
22 J. O. Sofo and G. D. Mahan, *Phys. Rev. B: Condens. Matter Mater. Phys.*, 1994, **49**, 4565–4570.
23 H. Şahin, S. Cahangirov, M. Topsakal, E. Bekaroglu, E. Akturk, R. T. Senger and S. Ciraci, *Phys. Rev. B: Condens. Matter Mater. Phys.*, 2009, **80**, 155453.
24 S. Froyen and W. A. Harrison, *Phys. Rev. B: Condens. Matter Mater. Phys.*, 1979, **20**, 2420–2422.
25 S. Zhang, M. Xie, F. Li, Z. Yan, Y. Li, E. Kan, W. Liu, Z. Chen and H. Zeng, *Angew. Chem., Int. Ed.*, 2016, **55**, 1666–1669.
26 Y. Pei, H. Wang and G. J. Snyder, *Adv. Mater.*, 2012, **24**, 6125–6135.
27 L.-D. Zhao, S.-H. Lo, Y. Zhang, H. Sun, G. Tan, C. Uher, C. Wolverton, V. P. Dravid and M. G. Kanatzidis, *Nature*, 2014, **508**, 373–377.
28 S. T. Pantelides and W. A. Harrison, *Phys. Rev. B: Solid State*, 1975, **11**, 3006–3021.
29 A. J. Mannix, X.-F. Zhou, B. Kiraly, J. D. Wood, D. Alducin, B. D. Myers, X. Liu, B. L. Fisher, U. Santiago, J. R. Guest, M. J. Yacaman, A. Ponce, A. R. Oganov, M. C. Hersam and N. P. Guisinger, *Science*, 2015, **350**, 1513–1516.
30 B. Feng, J. Zhang, Q. Zhong, W. Li, S. Li, H. Li, P. Cheng, S. Meng, L. Chen and K. Wu, *Nat. Chem.*, 2016, **8**(6), 563.
31 A. A. Balandin, S. Ghosh, W. Bao, I. Calizo, D. Teweldebrhan, F. Miao and C. N. Lau, *Nano Lett.*, 2008, **8**, 902–907.
32 L. Lindsay, D. A. Broido and N. Mingo, *Phys. Rev. B: Condens. Matter Mater. Phys.*, 2010, **82**, 115427.
33 Z. Ni, Q. Liu, K. Tang, J. Zheng, J. Zhou, R. Qin, Z. Gao, D. Yu and J. Lu, *Nano Lett.*, 2012, **12**, 113–118.
34 Z.-G. Shao, X.-S. Ye, L. Yang and C.-L. Wang, *J. Appl. Phys.*, 2013, **114**, 093712.
35 X.-S. Ye, Z.-G. Shao, H. Zhao, L. Yang and C.-L. Wang, *RSC Adv.*, 2014, **4**, 21216–21220.
36 B. Peng, H. Zhang, H. Shao, Y. Xu, R. Zhang, H. Lu, D. W. Zhang and H. Zhu, *ACS Appl. Mater. Interfaces*, 2016, **8**, 20977–20985.
37 V. O. Özçelik, O. U. Aktürk, E. Durgun and S. Ciraci, *Phys. Rev. B: Condens. Matter Mater. Phys.*, 2015, **92**, 125420.
38 Z. Zhu and D. Tománek, *Phys. Rev. Lett.*, 2014, **112**, 176802.
39 Y. Aierken, D. Çakir, C. Sevik and F. M. Peeters, *Phys. Rev. B: Condens. Matter Mater. Phys.*, 2015, **92**, 081408.
40 J. L. Zhang, S. Zhao, C. Han, Z. Wang, S. Zhong, S. Sun, R. Guo, X. Zhou, C. D. Gu, K. D. Yuan, Z. Li and W. Chen, *Nano Lett.*, 2016, **16**, 4903–4908.
41 S. Zhang, Z. Yan, Y. Li, Z. Chen and H. Zeng, *Angew. Chem., Int. Ed.*, 2015, **54**, 3112–3115.
42 G. Wang, R. Pandey and S. P. Karna, *ACS Appl. Mater. Interfaces*, 2015, **7**, 11490–11496.
43 O. U. Aktürk, V. O. Özçelik and S. Ciraci, *Phys. Rev. B: Condens. Matter Mater. Phys.*, 2015, **91**, 235446.
44 P. Ares, F. Aguilar-Galindo, D. Rodríguez-San-Miguel, D. A. Aldave, S. Díaz-Tendero, M. Alcamí, F. Martín, J. Gómez-Herrero and F. Zamora, *Adv. Mater.*, 2016, **28**, 6332–6336.
45 J. Ji, X. Song, J. Liu, Z. Yan, C. Huo, S. Zhang, M. Su, L. Liao, W. Wang, Z. Ni, Y. Hao and H. Zeng, *Nat. Commun.*, 2016, **7**, 13352.
46 X. Wu, Y. Shao, H. Liu, Z. Feng, Y.-L. Wang, J.-T. Sun, C. Liu, J.-O. Wang, Z.-L. Liu, S.-Y. Zhu, Y.-Q. Wang, S.-X. Du, Y.-G. Shi, K. Ibrahim and H.-J. Gao, *Adv. Mater.*, 2017, **29**, 1605407.
47 L. Li, Y. Yu, G. J. Ye, Q. Ge, X. Ou, H. Wu, D. Feng, X. H. Chen and Y. Zhang, *Nat. Nanotechnol.*, 2014, **9**, 372–377.
48 F. Xia, H. Wang and Y. Jia, *Nat. Commun.*, 2014, **5**, 4458.

49 A. Castellanos-Gomez, L. Vicarelli, E. Prada, J. O. Island, K. L. Narasimha-Acharya, S. I. Blanter, D. J. Groenendijk, M. Buscema, G. A. Steele, J. V. Alvarez, H. W. Zandbergen, J. J. Palacios and H. S. J. van der Zant, *2D Materials*, 2014, **1**, 025001.
50 J. R. Brent, N. Savjani, E. A. Lewis, S. J. Haigh, D. J. Lewis and P. O'Brien, *Chem. Commun.*, 2014, **50**, 13338–13341.
51 J. Qiao, X. Kong, Z.-X. Hu, F. Yang and W. Ji, *Nat. Commun.*, 2014, **5**, 4475.
52 C. Kamal and M. Ezawa, *Phys. Rev. B: Condens. Matter Mater. Phys.*, 2015, **91**, 085423.
53 R. Fei, A. Faghaninia, R. Soklaski, J.-A. Yan, C. Lo and L. Yang, *Nano Lett.*, 2014, **14**, 6393–6399.
54 G. Qin, Q.-B. Yan, Z. Qin, S.-Y. Yue, H.-J. Cui, Q.-R. Zheng and G. Su, *Sci. Rep.*, 2014, **4**, 6946.
55 H. Y. Lv, W. J. Lu, D. F. Shao and Y. P. Sun, *Phys. Rev. B: Condens. Matter Mater. Phys.*, 2014, **90**, 085433.
56 A. Castellanos-Gomez, *J. Phys. Chem. Lett.*, 2015, **6**, 4280–4291.
57 H. Du, X. Lin, Z. Xu and D. Chu, *J. Mater. Chem. C*, 2015, **3**, 8760–8775.
58 L. Kou, C. Chen and S. C. Smith, *J. Phys. Chem. Lett.*, 2015, **6**, 2794–2805.
59 E. Flores, J. R. Ares, A. Castellanos-Gomez, M. Barawi, I. J. Ferrer and C. Sánchez, *Appl. Phys. Lett.*, 2015, **106**, 022102.
60 J. Zhang, H. J. Liu, L. Cheng, J. Wei, J. H. Liang, D. D. Fan, P. H. Jiang, L. Sun and J. Shi, *J. Mater. Chem. C*, 2016, **4**, 991–998.
61 M. Akhtar, G. Anderson, R. Zhao, A. Alruqi, J. E. Mroczkowska, G. Sumanasekera and J. B. Jasinski, *NPJ 2D Mater. Appl.*, 2017, **1**, 5.
62 Y. Zhang, Y. Zheng, K. Rui, H. H. Hng, K. Hippalgaonkar, J. Xu, W. Sun, J. Zhu, Q. Yan and W. Huang, *Small*, 2017, **13**, 1700661.
63 L. Zhu, G. Zhang and B. Li, *Phys. Rev. B: Condens. Matter Mater. Phys.*, 2014, **90**, 214302.
64 A. Jain and A. J. H. McGaughey, *Sci. Rep.*, 2015, **5**, 8501.
65 G. Qin, Q.-B. Yan, Z. Qin, S.-Y. Yue, M. Hu and G. Su, *Phys. Chem. Chem. Phys.*, 2015, **17**, 4854–4858.
66 G. Zheng, Y. Jia, S. Gao and S.-H. Ke, *Phys. Rev. B*, 2016, **94**, 155448.
67 Z.-Y. Ong, Y. Cai, G. Zhang and Y.-W. Zhang, *J. Phys. Chem. C*, 2014, **118**, 25272–25277.
68 Z. Luo, J. Maassen, Y. Deng, Y. Du, R. P. Garrelts, M. S. Lundstrom, P. D. Ye and X. Xu, *Nat. Commun.*, 2015, **6**, 8572.
69 H. Jang, J. D. Wood, C. R. Ryder, M. C. Hersam and D. G. Cahill, *Adv. Mater.*, 2015, **27**, 8017–8022.
70 J. Zhu, H. Park, J.-Y. Chen, X. Gu, H. Zhang, S. Karthikeyan, N. Wendel, S. A. Campbell, M. Dawber, X. Du, M. Li, J.-P. Wang, R. Yang and X. Wang, *Adv. Electron. Mater.*, 2016, **2**, 1600040.
71 B. Sun, X. Gu, Q. Zeng, X. Huang, Y. Yan, Z. Liu, R. Yang and Y. K. Koh, *Adv. Mater.*, 2017, **29**, 1603297.
72 R. Fei and L. Yang, *Nano Lett.*, 2014, **14**, 2884–2889.
73 Z. Zhang, J. Xie, D. Yang, Y. Wang, M. Si and D. Xue, *Appl. Phys. Express*, 2015, **8**, 055201.
74 X. Ling, H. Wang, S. Huang, F. Xia and M. S. Dresselhaus, *Proc. Natl. Acad. Sci. U. S. A.*, 2015, **112**, 4523–4530.
75 K.-X. Chen, S.-S. Lyu, X.-M. Wang, Y.-X. Fu, Y. Heng and D.-C. Mo, *J. Phys. Chem. C*, 2017, **121**, 13035–13042.
76 J. Carrete, L. J. Gallego and N. Mingo, *J. Phys. Chem. Lett.*, 2017, **8**, 1375–1380.
77 Z. Zhu, J. Guan and D. Tománek, *Nano Lett.*, 2015, **15**, 6042–6046.
78 D. Kecik, E. Durgun and S. Ciraci, *Phys. Rev. B*, 2016, **94**, 205409.
79 J. Xi, M. Long, L. Tang, D. Wang and Z. Shuai, *Nanoscale*, 2012, **4**, 4348–4369.
80 M.-Q. Long, L. Tang, D. Wang, L. Wang and Z. Shuai, *J. Am. Chem. Soc.*, 2009, **131**, 17728–17729.
81 M. Long, L. Tang, D. Wang, Y. Li and Z. Shuai, *ACS Nano*, 2011, **5**, 2593–2600.
82 J. Xiao, M. Long, X. Zhang, J. Ouyang, H. Xu and Y. Gao, *Sci. Rep.*, 2015, **5**, 9961.
83 J. Xiao, M. Long, X. Zhang, D. Zhang, H. Xu and K. S. Chan, *J. Phys. Chem. Lett.*, 2015, **6**, 4141–4147.
84 J. Xiao, M. Long, C.-S. Deng, J. He, L.-L. Cui and H. Xu, *J. Phys. Chem. C*, 2016, **120**, 4638–4646.
85 B. Zeng, M. Li, X. Zhang, Y. Yi, L. Fu and M. Long, *J. Phys. Chem. C*, 2016, **120**, 25037–25042.
86 J. Bardeen and W. Shockley, *Phys. Rev.*, 1950, **80**, 72–80.
87 S. Kumar and U. Schwingenschlögl, *Chem. Mater.*, 2015, **27**, 1278–1284.
88 A. N. Gandi, H. N. Alshareef and U. Schwingenschlögl, *Chem. Mater.*, 2016, **28**, 1647–1652.
89 J. Yang, H. Li, T. Wu, W. Zhang, L. Chen and J. Yang, *Adv. Funct. Mater.*, 2008, **18**, 2880–2888.
90 A. J. Hong, J. J. Gong, L. Li, Z. B. Yan, Z. F. Ren and J.-M. Liu, *J. Mater. Chem. C*, 2016, **4**, 3281–3289.
91 M. Cutler and N. F. Mott, *Phys. Rev.*, 1969, **181**, 1336–1340.
92 F. Q. Wang, S. Zhang, J. Yu and Q. Wang, *Nanoscale*, 2015, **7**, 15962–15970.
93 H. Guo, T. Yang, P. Tao, Y. Wang and Z. Zhang, *J. Appl. Phys.*, 2013, **113**, 013709.
94 S. Bhattacharyya, T. Pandey and A. K. Singh, *Nanotechnology*, 2014, **25**, 465701.
95 L.-D. Zhao, S.-H. Lo, J. He, H. Li, K. Biswas, J. Androulakis, C.-I. Wu, T. P. Hogan, D.-Y. Chung, V. P. Dravid and M. G. Kanatzidis, *J. Am. Chem. Soc.*, 2011, **133**, 20476–20487.
96 Y.-L. Pei, J. He, J.-F. Li, F. Li, Q. Liu, W. Pan, C. Barreteau, D. Berardan, N. Dragoe and L.-D. Zhao, *NPG Asia Mater.*, 2013, **5**, e47.
97 H.-S. Kim, Z. M. Gibbs, Y. Tang, H. Wang and G. J. Snyder, *APL Mater.*, 2015, **3**, 041506.
98 J. Carrete, W. Li, L. Lindsay, D. A. Broido, L. J. Gallego and N. Mingo, *Mater. Res. Lett.*, 2016, **4**, 204–211.
99 B. Peng, D. Zhang, H. Zhang, H. Shao, G. Ni, Y. Zhu and H. Zhu, *Nanoscale*, 2017, **9**, 7397.
100 Y. Le Page and P. Saxe, *Phys. Rev. B: Condens. Matter Mater. Phys.*, 2002, **65**, 104104.

101 X. Wu, D. Vanderbilt and D. R. Hamann, *Phys. Rev. B: Condens. Matter Mater. Phys.*, 2005, **72**, 035105.
102 M. N. Blonsky, H. L. Zhuang, A. K. Singh and R. G. Hennig, *ACS Nano*, 2015, **9**, 9885–9891.
103 H. Shao, X. Tan, J. Jiang and H. Jiang, *EPL*, 2016, **113**, 26001.
104 T. Nakashima and Y. Umakoshi, *Philos. Mag. Lett.*, 1992, **66**, 317–321.
105 W. Kim, *J. Mater. Chem. C*, 2015, **3**, 10336–10348.
106 S. Lee, K. Esfarjani, T. Luo, J. Zhou, Z. Tian and G. Chen, *Nat. Commun.*, 2014, **5**, 3525.
107 C. W. Li, J. Hong, A. F. May, D. Bansal, S. Chi, T. Hong, G. Ehlers and O. Delaire, *Nat. Phys.*, 2015, **11**, 1063–1069.
108 J. P. Heremans, *Nat. Phys.*, 2015, **11**, 990–991.
109 X. Wu, V. Varshney, J. Lee, T. Zhang, J. L. Wohlwend, A. K. Roy and T. Luo, *Nano Lett.*, 2016, **16**, 3925–3935.
110 E. J. Skoug and D. T. Morelli, *Phys. Rev. Lett.*, 2011, **107**, 235901.
111 Y. Zhang, E. Skoug, J. Cain, V. Ozoliņš, D. Morelli and C. Wolverton, *Phys. Rev. B: Condens. Matter Mater. Phys.*, 2012, **85**, 054306.
112 W. Lai, Y. Wang, D. T. Morelli and X. Lu, *Adv. Funct. Mater.*, 2015, **25**, 3648–3657.
113 G. Tan, W. G. Zeier, F. Shi, P. Wang, G. J. Snyder, V. P. Dravid and M. G. Kanatzidis, *Chem. Mater.*, 2015, **27**, 7801–7811.
114 L.-D. Zhao, J. He, S. Hao, C.-I. Wu, T. P. Hogan, C. Wolverton, V. P. Dravid and M. G. Kanatzidis, *J. Am. Chem. Soc.*, 2012, **134**, 16327–16336.
115 D. M. Rowe, V. S. Shukla and N. Savvides, *Nature*, 1981, **290**, 765–766.
116 K. Biswas, J. He, I. D. Blum, C.-I. Wu, T. P. Hogan, D. N. Seidman, V. P. Dravid and M. G. Kanatzidis, *Nature*, 2012, **489**, 414–418.
117 Y. Lee, S.-H. Lo, J. Androulakis, C.-I. Wu, L.-D. Zhao, D.-Y. Chung, T. P. Hogan, V. P. Dravid and M. G. Kanatzidis, *J. Am. Chem. Soc.*, 2013, **135**, 5152–5160.
118 J. Zhang, H. J. Liu, L. Cheng, J. Wei, J. H. Liang, D. D. Fan, P. H. Jiang and J. Shi, *Sci. Rep.*, 2017, **7**, 4623.
119 M. Zeraati, S. M. Vaez Allaei, I. Abdolhosseini Sarsari, M. Pourfath and D. Donadio, *Phys. Rev. B*, 2016, **93**, 085424.
120 G. Qin, X. Zhang, S.-Y. Yue, Z. Qin, H. Wang, Y. Han and M. Hu, *Phys. Rev. B*, 2016, **94**, 165445.
121 B. Peng, H. Zhang, H. Shao, Y. Xu, X. Zhang and H. Zhu, *Ann. Phys.*, 2016, **528**, 504–511.
122 B. Peng, Z. Ning, H. Zhang, H. Shao, Y. Xu, G. Ni and H. Zhu, *J. Phys. Chem. C*, 2016, **120**, 29324–29331.
123 B. Peng, H. Zhang, H. Shao, Y. Xu, G. Ni, R. Zhang and H. Zhu, *Phys. Rev. B*, 2016, **94**, 245420.
124 Y. Chen, T. Jayasekera, A. Calzolari, K. W. Kim and M. B. Nardelli, *J. Phys.: Condens. Matter*, 2010, **22**, 372202.
125 X.-M. Wang, D.-C. Mo and S.-S. Lu, *J. Chem. Phys.*, 2013, **138**, 204704.
126 H. Sevincli and C. Sevik, *Appl. Phys. Lett.*, 2014, **105**, 223108.
127 X. Tan, H. Shao, T. Hu, G. Liu, J. Jiang and H. Jiang, *Phys. Chem. Chem. Phys.*, 2015, **17**, 22872–22881.
128 T. Ouyang, H. Xiao, Y. Xie, X. Wei, Y. Chen and J. Zhong, *J. Appl. Phys.*, 2013, **114**, 073710.
129 T. Ouyang and M. Hu, *Nanotechnology*, 2014, **25**, 245401.
130 W.-X. Zhou and K.-Q. Chen, *Carbon*, 2015, **85**, 24–27.
131 Z. Yang, Y.-L. Ji, G. Lan, L.-C. Xu, H. Wang, X. Liu and B. Xu, *J. Phys. D: Appl. Phys.*, 2016, **49**, 145102.
132 X.-M. Wang and S.-S. Lu, *J. Phys. Chem. C*, 2013, **117**, 19740–19745.
133 G. Kresse and J. Furthmüller, *Phys. Rev. B: Condens. Matter Mater. Phys.*, 1996, **54**, 11169–11186.
134 L. Chaput, P. Pécheur and H. Scherrer, *Phys. Rev. B: Condens. Matter Mater. Phys.*, 2007, **75**, 045116.
135 M. Omini and A. Sparavigna, *Phys. Rev. B: Condens. Matter Mater. Phys.*, 1996, **53**, 9064–9073.
136 W. Li, N. Mingo, L. Lindsay, D. A. Broido, D. A. Stewart and N. A. Katcho, *Phys. Rev. B: Condens. Matter Mater. Phys.*, 2012, **85**, 195436.
137 W. Li, L. Lindsay, D. A. Broido, D. A. Stewart and N. Mingo, *Phys. Rev. B: Condens. Matter Mater. Phys.*, 2012, **86**, 174307.
138 W. Li, J. Carrete and N. Mingo, *Appl. Phys. Lett.*, 2013, **103**, 253103.
139 S. Baroni, S. de Gironcoli, A. Dal Corso and P. Giannozzi, *Rev. Mod. Phys.*, 2001, **73**, 515–562.